Spectroscopic follow-up of a cluster candidate at $z = 1.45$

Caroline van Breukelen,[1][*] Garret Cotter,[1] Steve Rawlings,[1] Tony Readhead,[2]
David Bonfield,[1][†] Lee Clewley,[1] Rob Ivison,[3,4] Matt Jarvis,[5]
Chris Simpson,[6] Mike Watson[7]

[1] *Astrophysics, Department of Physics, Keble Road, Oxford, OX1 3RH, UK*
[2] *Owens Valley Radio Observatory, California Institute of Technology, Pasadena, CA 91125, USA*
[3] *UK Astronomy Technology Centre, Royal Observatory, Blackford Hill, Edinburgh EH9 3HJ*
[4] *Scottish Universities Physics Alliance, Institute for Astronomy, University of Edinburgh, Blackford Hill, Edinburgh EH9 3HJ*
[5] *Centre for Astrophysics, Science & Technology Research Institute, University of Hertfordshire, Hatfield, AL10 9AB, UK*
[6] *Astrophysics Research Institute, Liverpool John Moores University, Twelve Quays House, Egerton Wharf, Birkenhead CH41 1LD, UK*
[7] *X-ray Astronomy Group, Department of Physics and Astronomy, University of Leicester, Leicester LE1 7RH, UK*

Released 2007 Xxxxx XX

ABSTRACT

We have obtained deep optical spectroscopic data of the highest-redshift cluster candidate ($z \sim 1.4$, CVB13) selected by Van Breukelen et al. (2006) in a photometric optical/infrared catalogue of the Subaru XMM-Newton Deep Field. The data, which comprise 104 targeted galaxies, were taken with the DEep Imaging Multi-Object Spectrograph (DEIMOS) on the Keck 2 telescope and yielded 31 secure redshifts in the range $1.25 < z < 1.54$ within a $7' \times 4'$ field centred on CVB13. Instead of one massive cluster at $z = 1.4$, we find evidence for three projected structures at $z = 1.40$, $z = 1.45$, and $z = 1.48$. The most statistically robust of these structures, at $z = 1.454$, has six spectroscopically confirmed galaxies. Its total mass is estimated at $\gtrsim 10^{14} \mathrm{M}_\odot$ and it may therefore be termed a cluster. There is an X-ray source at the cluster position which is marginally spatially resolved but whose X-ray spectrum is too hard to be thermal cluster emission. Its origin could be the summed X-ray emission from active galaxies in, and projected onto, the cluster. Serendipitously we have discovered a cluster at $z = 1.28$ with a mass of $\gtrsim 10^{14} \mathrm{M}_\odot$ at the same position on the sky, comprising six spectroscopically confirmed cluster galaxies and at least one additional radio source. The selection of CVB13 for the cluster catalogue was evidently aided by the superposition of other, presumably lower-mass, structures, whereas the single cluster at $z = 1.28$ contained too few galaxies to be isolated by the same algorithm. Given the complicated nature of such structures, caution must be employed when measuring the mass function of putative high-redshift clusters with photometric techniques alone.

Key words: galaxies: clusters: general – galaxies: high-redshift – radio continuum: general – X-rays: galaxies – X-rays: galaxies: clusters

1 INTRODUCTION

Clusters of galaxies are important probes for both cosmology and astrophysics. They are the most massive virialised structures in the Universe, and they are therefore excellent targets to study large-scale structure formation. The cluster mass function directly links to the normalisation of the power spectrum of density perturbations, σ_8, which is the RMS in the density on a scale of $8h^{-1}$ Mpc

($h = H_0/100 \, \mathrm{km \, s^{-1} Mpc^{-1}}$). The evolution of the mass function with redshift reflects the growth function of the Universe, which is determined by Ω_M (the matter density parameter), Ω_Λ (the dark energy density parameter), and w (the dark energy equation-of-state parameter). Further, clusters are of great interest to astrophysics because they can be approximated by a 'closed-box' environment. This makes them ideal laboratories to study the interaction of galaxies and the intergalactic medium, which is thought to play a large role in galaxy formation and evolution. An important remaining question is why so little baryonic matter in clusters forms stars (e.g. Cole 1991; White & Frenk 1991). Feedback processes coupling baryonic matter from galaxies to the

---

[*] Email: cvb@astro.ox.ac.uk
[†] Now at NASA's Goddard Space Flight Center, Greenbelt, MD 20771, USA.

intergalactic medium are likely to counter further condensation of the intergalactic gas and halt star-formation. Two examples of these processes are galactic winds due to multiple supernovae in star-burst galaxies (e.g. Heckman 2002) and outflow from radio-loud AGN (e.g. Scannapieco & Oh 2004; Fabian, Celotti & Erlund 2006a).

Cluster searches have been carried out for decades. The first extensive cluster catalogue was created by Abell (Abell 1958; Abell et al. 1989). Unfortunately Abell only had single-filter photographic plates at his disposal and therefore his work was severely complicated by projection effects. Gladders et al. (1998) improved upon this situation by showing that a redshift estimate can be determined by using only two filters and targeting the bright, red elliptical galaxy population in clusters which form the red sequence (e.g. Bower, Lucey & Ellis 1992). A particularly important advance in optical cluster detection has come from the advent of large arrays of CCD detectors allowing large surveys to be carried out efficiently, such as the relatively shallow (z < 0.4) but very wide-field Sloan Digital Sky Survey (SDSS) (e.g Goto et al. 2002; Kim et al. 2002; Miller et al. 2005). There have been numerous smaller-area surveys to higher redshifts, for example the Palomar Distant Cluster Survey (Postman et al. 1996), the ESO Imaging Survey (Lobo et al. 2000), and the Red Sequence Cluster Survey (Gladders et al. 2005). Moving to even higher redshifts, proto-clusters have been found by focussing on fields around quasars or radio galaxies (e.g. Venemans et al. 2002) as a large fraction of these objects have been shown to reside in clusters (see Pascarelle et al. 1996; Röttgering et al. 1996). However, selecting clusters in blank sky surveys with optical photometry at redshifts $z \gtrsim 1$ was impractical for a long time because of the shifting of the 4000 Å break – characteristic for the red, passively evolving ellipticals predominantly found in clusters – out of the I-band to longer wavelength bands.

The launch of the *ROSAT* satellite in 1990 greatly advanced the study of clusters in the X-ray regime, enabling the discovery of hundreds of clusters up to $z \sim 1$. Later *Chandra* and *XMM-Newton* provided the possibility to observe even deeper owing to their unprecedented sensitivity and angular resolution. X-ray cluster surveys now extend well above $z \sim 1$ (e.g. Stanford et al. 2001; Rosati et al. 2004; Bremer et al. 2006). Stanford et al. (2006) currently hold the record of the most-distant spectroscopically-confirmed cluster at $z = 1.451$. This cluster was initially detected as an extended source in XMM X-ray data; spectroscopic follow-up revealed five cluster galaxies within a $1'$-diameter. The temperature of the intra-cluster medium (ICM) was shown to be ~ 7 keV, which is the highest detected in any cluster at $z > 1$, implying a relatively massive cluster for such a high redshift.

Another way to observe the ICM is through the Sunyaev-Zel'dovich effect (S-Z effect, Sunyaev & Zel'dovich 1970, 1972). This effect is visible as a distortion of the Cosmic Microwave Background (CMB): as the CMB-photons travel through the ICM they are subjected to inverse Compton scattering, which shifts the energies of a small fraction of the photons slightly upwards. In the last decade many detections have been made of the S-Z effect (e.g. Birkinshaw, 1999; Carlstrom et al. 2000, Jones et al. 2005) and comprehensive S-Z surveys are underway (Kneissl et al. 2001).

Cotter et al. (2002) used pointed S-Z observations to detect hot gas associated with a $z \sim 1$ cluster of radio sources.

Recent development of wide-field infrared cameras, such as the Wide-Field CAMera (WFCAM) on the United Kingdom InfraRed Telescope (UKIRT), have brought photometric cluster surveys back into vogue by enabling deep, large-scale infrared surveys and pushing the limit of photometric cluster selection to significantly higher redshifts. The UKIRT Infrared Deep Sky Survey (UKIDSS, Lawrence et al. 2006) is a suite of both wide and deep infrared imaging surveys using WFCAM. The Ultra Deep Survey is the deepest of these, and covers 0.8 deg^2 in the Subaru XMM-Newton Deep Field (SXDF, Sekiguchi et al. [in prep.]) with a planned limiting magnitude of $K_{\mathrm{Vega}} = 23$. Deep $BVRi'z'$ imaging data from the Subaru Telescope are also available on the SXDF (Furusawa et al. [in prep.]), as is X-ray data by XMM-Newton (Watson et al. 2004), radio data from the Very Large Array (Simpson et al. 2006, Ivison et al. 2007), and Spitzer infrared data ranging from 3.6 to 24 micron (Lonsdale et al. 2005).

We previously exploited these exceptional multi-wavelength datasets to execute a high-redshift cluster survey, using photometric redshifts, as reported in Van Breukelen et al. 2006 (VB06). In VB06 we isolated 13 cluster candidates at $0.6 < z < 1.4$ in 0.5 deg^2 of the SXDF. The highest-redshift cluster candidate, CVB13 (RA = $02^h18^m10.5^s$, Dec = -05°01′05″ [J2000]), was estimated to lie at $z = 1.39 \pm 0.07$.

In this paper we present the spectroscopic follow-up of the putative CVB13 cluster with the DEep Imaging Multi-Object Spectrograph (DEIMOS, Cowley et al. 1997) on the 10-metre Keck 2 telescope. Section 2 describes the observations and data reduction. The analysis and discussion on the nature of the system are given in Section 3. Section 4 contains concluding remarks. Throughout this paper we use $H_0 = 70 \,\mathrm{km\,s^{-1}Mpc^{-1}}$ ($h = 0.7$), $\Omega_{\mathrm{M}} = 0.3$, and $\Omega_\Lambda = 0.7$ and a ΛCDM power spectrum with $\sigma_8 = 0.75$; all sky coordinates are quoted in equinox J2000.

2   THE DATA

2.1   Selection of the targets

We selected four samples of target galaxies to create a Multi-Object Spectroscopy (MOS) mask. Each of these samples comprised groups of different priorities. The samples are described below; the masks were created by allocating the maximum number of slits to sample 1, priority 1, and moving down through all the priorities within the sample before allocating slits to the next sample.

Sample 1: This sample included all galaxies that were determined to be a possible cluster member of CVB13 by the algorithm described in VB06. The algorithm presented in this paper used two methods to detect clusters: Voronoi Tesselations and Friends-of-Friends. The galaxies that were assigned to the cluster by both methods composed the highest-priority target group within this sample. The second priority group comprised the cluster members as selected only by Friends-of-Friends, followed by the galaxies found only by Voronoi Tesselations, as this is a less reliable method to determine cluster membership (see VB06). The target list
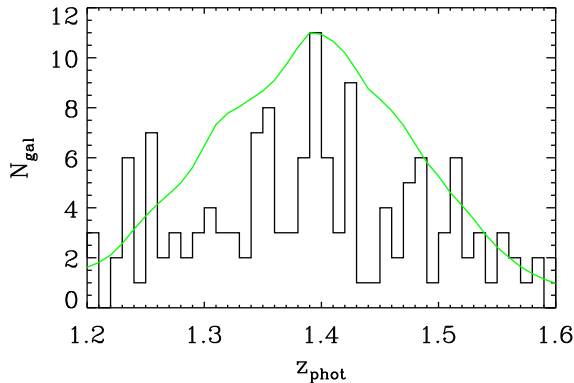
Figure 1. Histogram of the photometric redshifts of galaxies in the field of CVB13 ($02^h17^m54.6^s \leqslant$ RA $\leqslant 02^h18^m26.4^s$ and $-05°03'05'' \leqslant$ Dec $\leqslant -04°59'05''$ in the redshift range $1.2 < z < 1.6$. At $z = 1.4$ the projected region of interest has proper size $3.6 \times 2.0 \, \mathrm{Mpc}^2$. The photometric redshifts were calculated using Bruzual & Charlot (2003) modelled spectral energy distributions from stellar population synthesis (see VB06 for a discussion of the photometric redshifts). The solid line is the sum of the redshift probability functions (normalised to the peak of the histogram) of the galaxies with a photometric redshift within the shown redshift range.

of this sample consisted of a total of 125 objects, of which 18 objects of priority 1, 3 of priority 2, and 104 of priority 3. Slits could be placed on 61 of these 125 targets, divided into priorities 1: 10 galaxies, 2: 0 galaxies, and 3: 51 galaxies.

Sample 2: By rotating the DEIMOS instrument by 90 degrees we were able to utilise the long axis of the field-of-view to target another candidate cluster from VB06 within the same observations. This was cluster 6 (CVB6) at $z = 0.76 \pm 0.12$, RA $= 02^h18^m32.7^s$, Dec $= -05°01'04''$. The target galaxies for this sample were selected and prioritised exactly as for sample 1. There were 152 targets in total, divided into priorities 1: 30, 2: 1, 3: 121. Of these, 64 sources could be observed: 13 of priority 1, 1 of priority 2, and 50 of priority 3.

Sample 3: The third sample consisted of various active galaxies is the field, detected by their X-ray activity, radio emission, or excess flux in the Spitzer 24-μm band. We found 48 radio sources in the field, which made up priority group 1. The second priority group included 31 X-ray sources. The last priority group consisted of 12 objects with a detection in the 24-μm band and a colour of $J - K = 2$. The target list comprised 91 sources, of which 26 were observed (15 radio sources, 8 X-ray sources, 3 24-μm sources).

Sample 4: The final sample was designed to fill up all remaining slits in the two masks. It included all galaxies in the field with a photometric redshift of $1.25 < z_{phot} < 1.54$. Fig. 1 is a histogram of the photometric redshifts of these objects; overplotted is the sum of their redshift probability distribution functions. The chosen redshift range corresponds to the $\pm$ 2-sigma range on the photometric redshift of the cluster candidate CVB13. This error on the cluster redshift reflects the combined redshift probability distribution functions of the cluster candidate members as given in VB06. This sample consisted of 1139 objects of which 43 were observed.

2.2 Observations and data reduction

Optical spectroscopy was undertaken on the 21st of December 2006 using the DEIMOS instrument on the Keck 2 telescope. The telescope was pointed at RA $= 02^h18^m20.00^s$, Dec $= -05°01'04.9''$ and the field-of-view of the instrument, with a position angle of $90°$, was $16.7' \times 5'$ in RA $\times$ Dec. The two MOS masks comprised one-arcsecond wide slits. The 600 line mm^{-1} grating was used in conjunction with the GG495 order-blocking filter. A long-slit observation of Feige 110 was taken for spectrophotometric calibration. Four 1800-s integrations were taken for each mask, and short-exposure images were taken through the mask after each spectroscopic integration to ensure mask alignment. Seeing, as measured on the alignment images, varied between $0.6''$ and $1.0''$. Conditions were photometric throughout.

The two-dimensional spectra were reduced with the DEEP2 DEIMOS Data Pipeline[1]. The pipeline processes the flats and arcs to determine the position of the slitlets on the CCD and to find the two-dimensional wavelength solution for each slitlet. Subsequently the spectra are flat-field corrected and the curvature of the spectra in the spatial direction is rectified. The separate science exposures are sky-subtracted and finally combined into one mean, cosmic-ray rejected, science frame.

We extracted the one-dimensional spectra with a box-car extraction routine, using a $0.8''$-width aperture. To enable flux calibration, the standard star longslit exposure was reduced with the IRAF package 'twodspec'. The sensitivity function was determined using the IRAF task 'sensfunc' and the one-dimensional science spectra were calibrated with the task 'calibrate'. We note that for the average seeing of $0.8''$ we missed ~ 13 per cent of a typical galaxy's flux within our aperture.

2.3 The spectroscopic sample

Overall the two MOS masks targeted 194 objects. Of these, we were able to assign redshifts to 139 galaxies (72 per cent), which were divided over the samples as follows: 38 redshifts in sample 1, 57 redshifts in sample 2, 23 redshifts in sample 3, and 21 redshifts in sample 4. The remaining 28 per cent of the observed galaxies had continua too faint to allow a redshift determination from absorption features and showed no emission lines. Fig. 2 shows the positions of the targets within the DEIMOS field-of-view where each sample is depicted in a different colour.

In this paper we focus solely on cluster candidate CVB13. We therefore imposed two selection criteria to create our final spectroscopic sample: i) the objects had to be within the $7' \times 4'$ field centred on RA $= 02^h18^m10.5^s$ and Dec $= -05°01'05''$ (see Fig. 1 caption for RA and Dec limits of the sample); ii) the redshift range was restricted to $1.25 < z < 1.54$, which was the original 2-sigma range of cluster candidate redshift (see Section 2.1). There were 30 objects in our DEIMOS data that satisfied these criteria, of which 25 were from target-sample 1 and 5 from target-sample 4. These objects are shown in Fig. 2 with red circles. We added one galaxy to our final sample that was observed

---

[1] http://astro.berkeley.edu/~cooper/deep/spec2d/
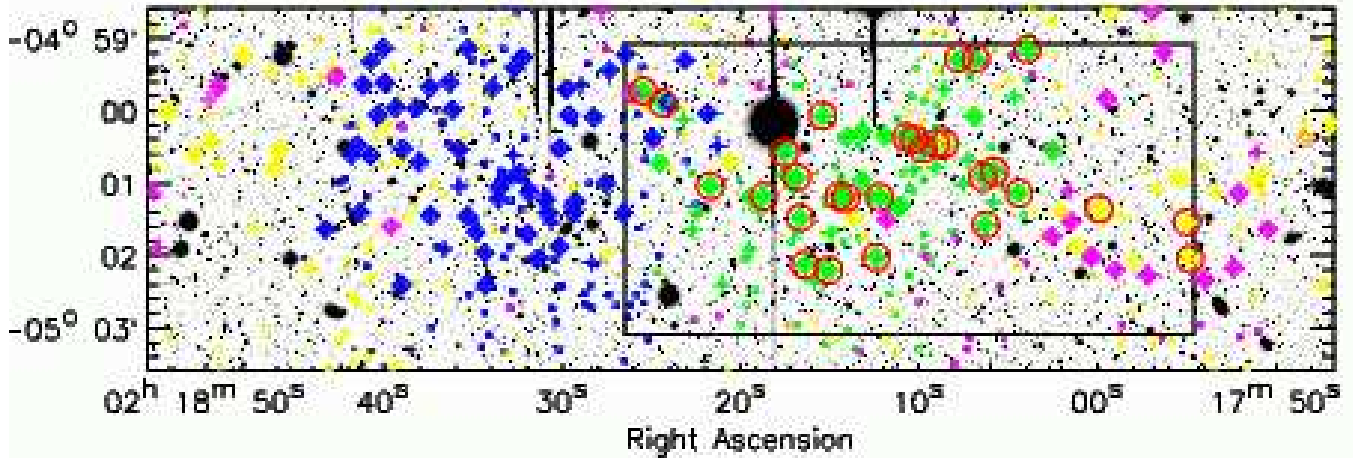
Figure 2. Spectroscopy targets overlaid on the i'-band image (Furusawa et al. [in prep.]) of the DEIMOS field-of-view. Sample 1 is depicted in green symbols, sample 2 in blue, sample 3 in purple, and sample 4 in yellow (see Section 2.1). The small squares symbolise all the objects in the target list, the plusses are the objects that were actually observed, and the diamonds are all the targets for which a redshift could be determined. The red circles are the objects which are included in the final spectroscopic sample for this paper: they fall within the depicted box of $7' \times 4'$ centred on RA = $02^h18^m10.5^s$, Dec = -05°01′05″ and have redshifts of $1.25 < z < 1.54$ (see Section 2.3).

with the Gemini Multi-Object Spectrograph (GMOS, Hook et al. 2004) on the Gemini North Telescope in Hawaii and satisfied the same selection criteria. The respective sample selection and data description can be found in Van Breukelen et al. (in prep.). This brought the total of the final spectroscopic sample to 31 objects.

3   ANALYSIS AND DISCUSSION

3.1   Properties of the line emitters

Due to the high redshift of our spectroscopic sample of 31 galaxies, the continua of the spectra are weak, rendering redshift determination by absorption features alone unfeasible. All redshifts in the final sample were therefore calculated from the [O II] emission line at 3727 Å. The identification of the [O II] line is reliable because in some cases the doublet was resolved, in others there were supporting absorption features, or there were no other emission lines visible within the spectral range that would be expected if the [O II] line was actually another emission line at a different redshift. The one- and two-dimensional spectra of the detected emission lines are shown in Fig. 3, where the identified line features are labelled and noisy sky regions are shaded. The three-dimensional distribution of the galaxies within our target area is depicted in Fig. 4 in comoving coordinates (X corresponds to RA, Y to Dec and z to redshift). The galaxies are colour-coded to redshift, from blue at $z = 1.25$ to red at $z = 1.53$.

To determine the exact redshift, the line flux and the equivalent width of the [O II] emitters, we fit a line profile to the [O II] emission line in each object. As the [O II]$_{3727}$ line is a doublet, the fitted line profile consists of two Gaussians at $\lambda_{rest} = 3726.1$ Å and $\lambda_{rest} = 3728.8$ Å. The Full Width Half Maximum (FWHM) of each Gaussian is assumed to be equal, and is a free parameter of the fitted function. The other parameters are the redshift, the continuum level, and

the ratio of fluxes of the two lines. The flux ratio is constrained to be within the limits for high and low density (Osterbrock 1967), corresponding to $0.35 \leqslant F_{3729}/F_{3726} \leqslant 1.5$, where F is the single line flux. Random errors on the flux and redshift measurement are determined by fitting modelled lines with the same procedure.

We calculate the Star-Formation Rate (SFR) of the galaxies using the equation given by Kennicutt (1998):

$$\mathrm{SFR} = (1.4 \pm 0.4) \times 10^{-34} L_{[\mathrm{O\,II}]}, \qquad (1)$$

where the SFR is in $M_\odot\,\mathrm{yr}^{-1}$ and $L_{[\mathrm{O\,II}]}$ is the luminosity of the [O II]$_{3727}$ emission line in Watts. This equation assumes $L_{[\mathrm{O\,II}]}/L_{\mathrm{H}\alpha} = 0.57$ and a Salpeter initial mass function with stellar masses between 0.1 and 100 $M_\odot$. Extinction or total obscuration is not corrected for and therefore these estimates represent lower limits on the SFR. The properties of the complete sample can be found in Table 1. In this table the redshift has been converted to heliocentric redshift (see Danese, De Zotti & Di Tullio 1980).

3.2   Sample completeness

To estimate the completeness of our spectroscopic sample, we have to take three factors into account:

(i) The original target list was compiled from the UKIDSS-UDS Early Data Release (EDR) catalogue, which has a limiting K-band magnitude of $K_{\mathrm{Vega}} = 20.6$. Cirasuolo et al. (2006) present a K-band luminosity function of galaxies in the UKIDSS-UDS in different redshift bins. We can calculate the total expected number of galaxies using their Schechter function for redshift range $1.25 < z < 1.50$, characterised by $\phi^* = 2.6 \pm 0.3 \times 10^{-3}\mathrm{Mpc}^{-3}$, $M^*_{K,\mathrm{Vega}} = -24.93 \pm 0.16$, and $\alpha = -0.92 \pm 0.18$. In our field of $7' \times 4'$ and $1.25 < z < 1.54$ we would expect 391 galaxies in total; when we impose the magnitude limit of $K_{\mathrm{Vega}} = 20.6$ we would only expect to detect 99 objects, or 25 per cent.
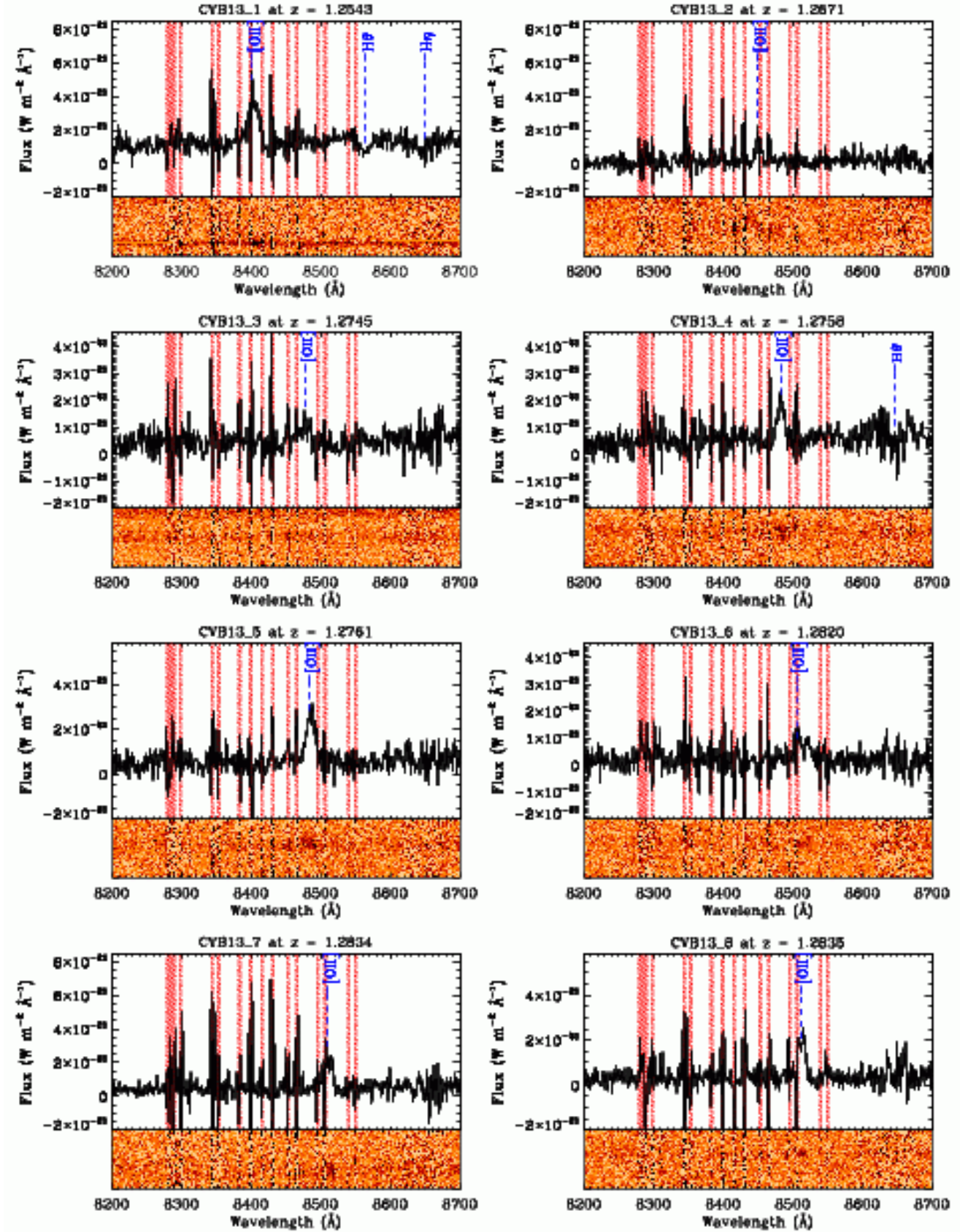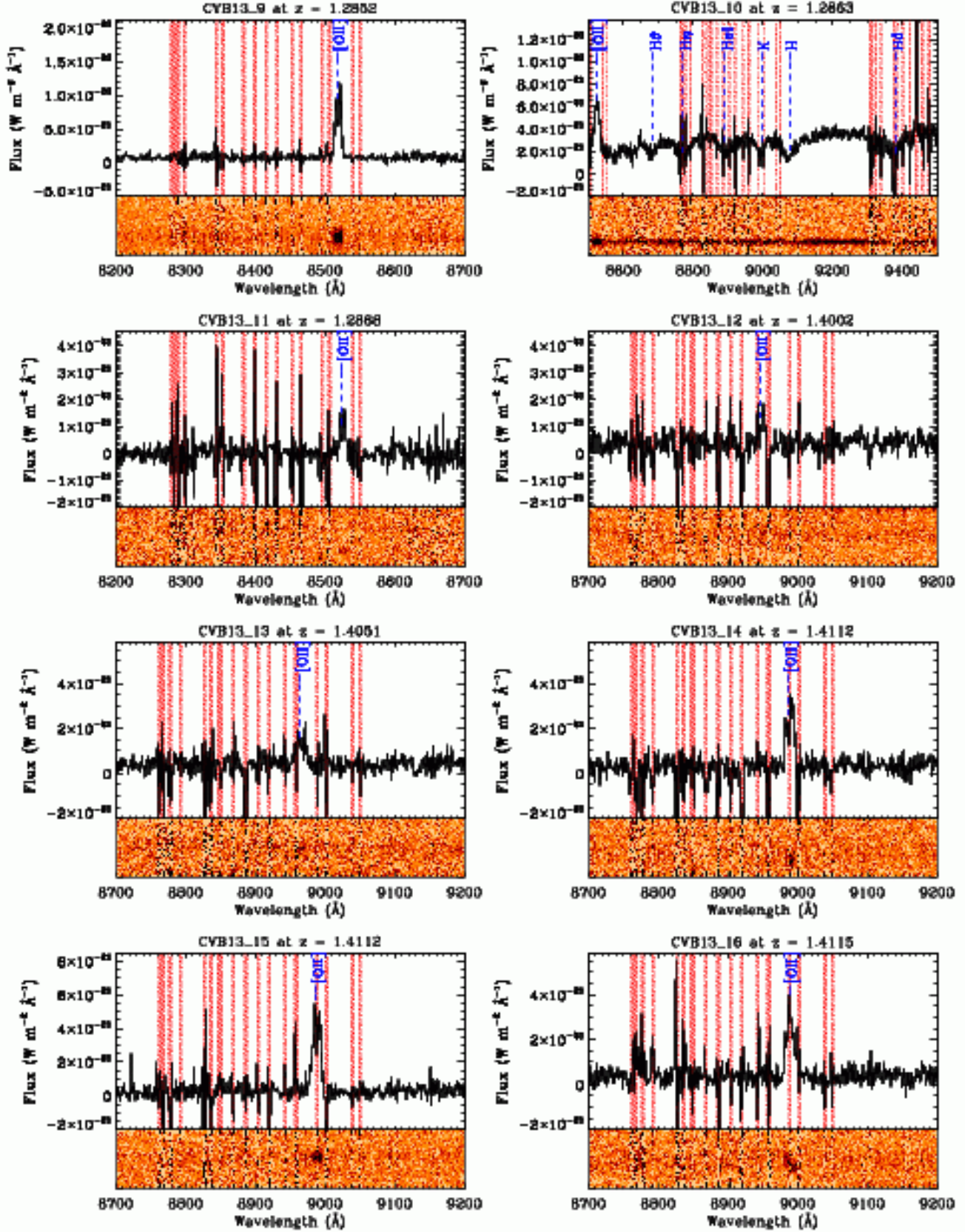
Figure 3. One-dimensional and two-dimensional DEIMOS spectra of the galaxies in the field of CVB13. Identified emission and absorption features are labelled. The shaded regions denote noisy parts of the spectra due to sky lines.

Figure 3 cont'd. One-dimensional and two-dimensional DEIMOS spectra of the galaxies in the field of CVB13. Identified emission and absorption features are labelled. The shaded regions denote noisy parts of the spectra due to sky lines.

Figure 3 cont'd. One-dimensional and two-dimensional DEIMOS spectra of the galaxies in the field of CVB13. Identified emission and absorption features are labelled. The shaded regions denote noisy parts of the spectra due to sky lines.
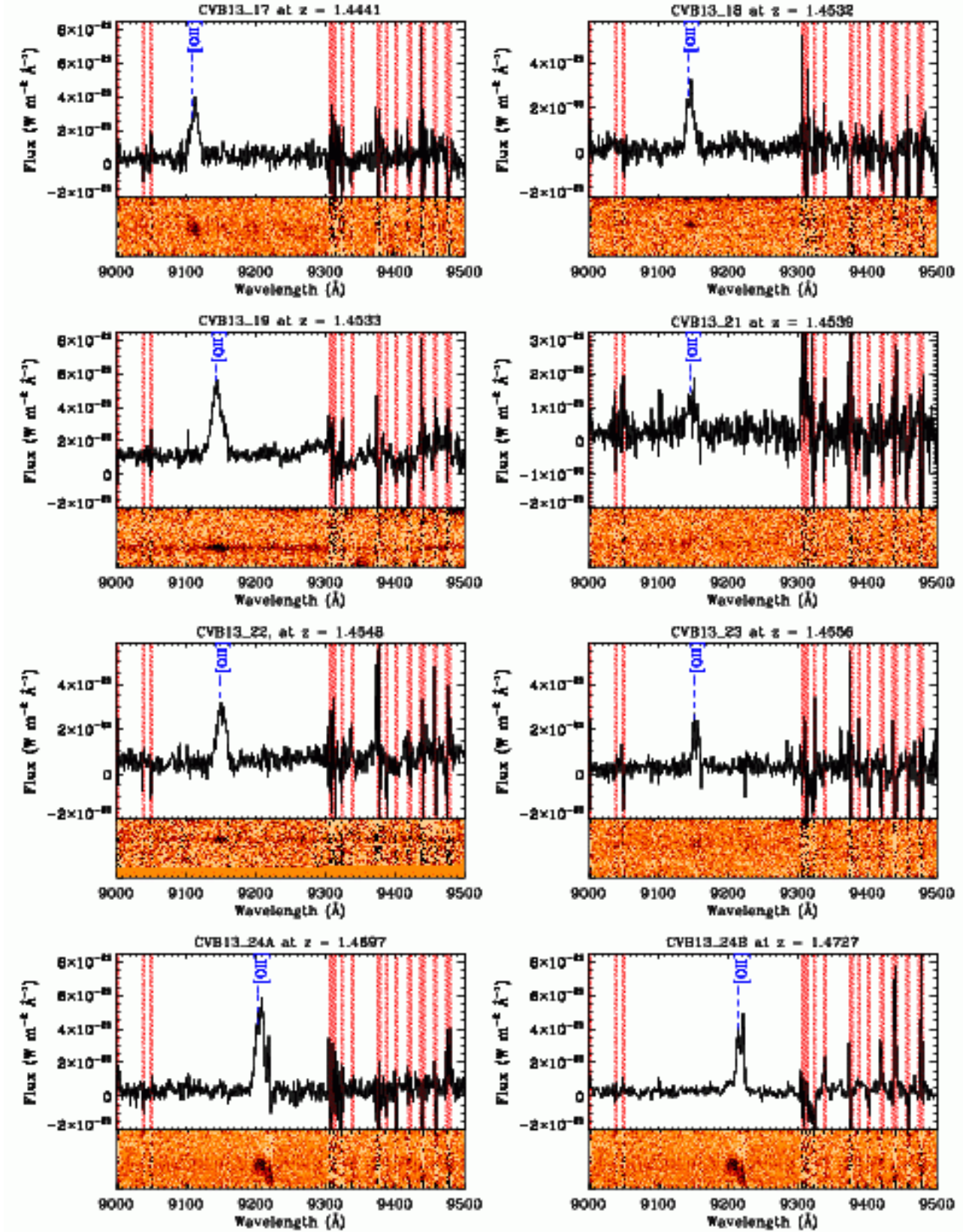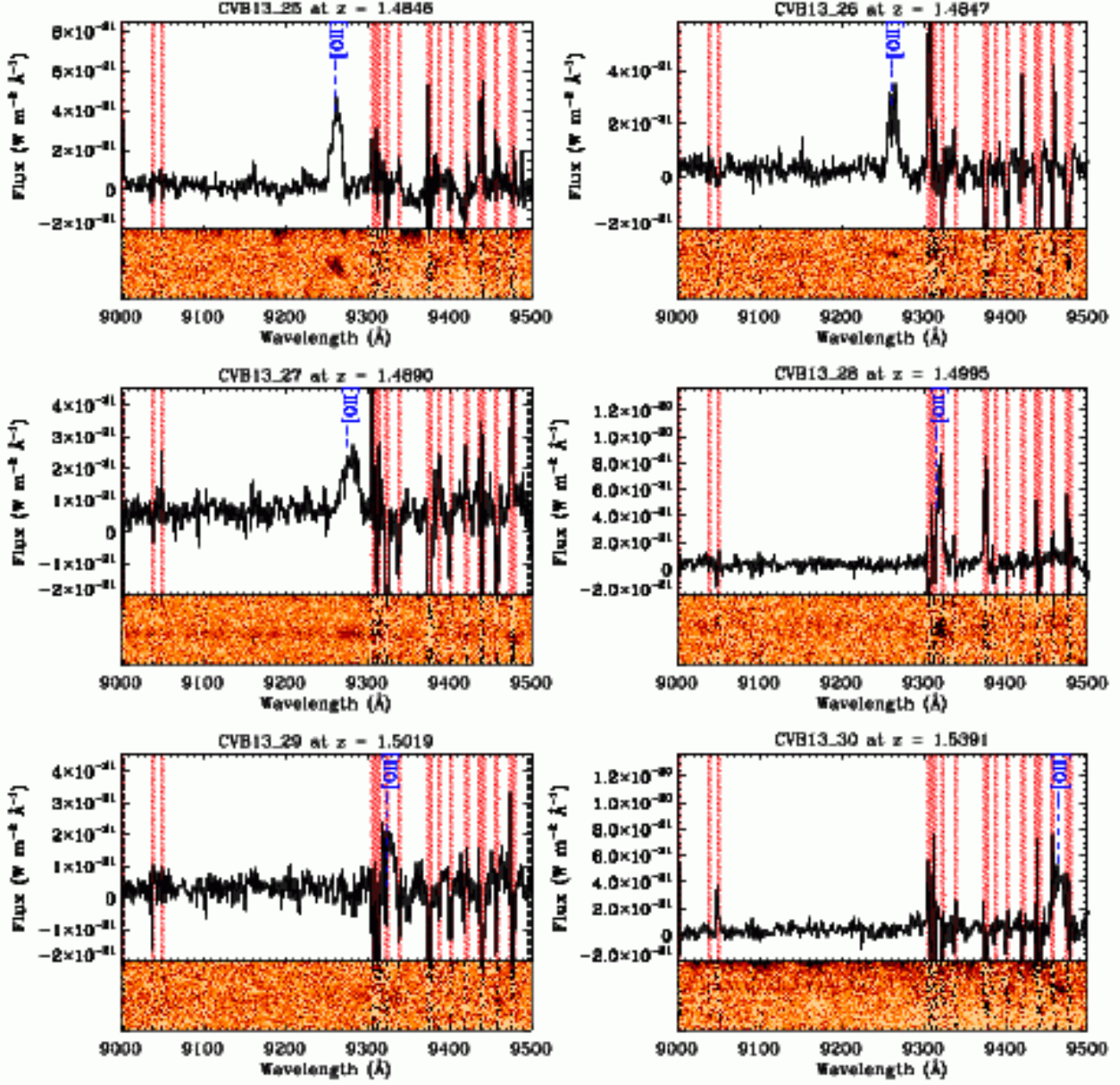
Figure 3 cont'd. One-dimensional and two-dimensional DEIMOS spectra of the galaxies in the field of CVB13. Identified emission and absorption features are labelled. The shaded regions denote noisy parts of the spectra due to sky lines.

(ii) The nature of a MOS mask makes complete sampling of the target list impossible. Out of our original target list 177 objects satisfied our selection criteria (see Section 2.1), using photometric redshifts for the redshift criterion of $1.25 < z < 1.54$. Of these objects, 75 were observed with the MOS masks. This means our spectroscopic data sampled 42 per cent of the galaxies we intended to target.

(iii) All the objects in our sample are [O II] emitters. We only detect the [O II] lines with a line flux $> 1.0 \times 10^{34}\,\mathrm{W\,m^{-2}}$. Furthermore, sky lines raise the flux limit of the [O II] line that we can detect in specific parts of the spectra. However, this affects lines with different line widths in different ways. We determine our detection completeness of [O II] lines with a flux greater than the flux limit of $1.0 \times 10^{34}\,\mathrm{W\,m^{-2}}$ by modelling a two-dimensional

[O II]$_{3727}$ line. The modelled lines have a rest-frame FWHM varying between 1.3 and 7.6 Å and fluxes from 10^{-20} to $10^{-19}\,\mathrm{W\,m^{-2}}$, corresponding to the range of observed rest-frame FWHMs and line fluxes. We add the modelled lines at redshifts of $1.25 \leqslant z \leqslant 1.54$ to a two-dimensional sky frame and try to recover the lines with the same procedure as used for the real spectra. Assuming a uniform distribution over the FWHM range and a Schechter distribution in flux, we calculate the fraction of missed sources at each redshift bin to find the detection completeness of [O II] lines with flux $> 1.0 \times 10^{34}\,\mathrm{W\,m^{-2}}$. The result ranges from 22 per cent at the locations of the strongest sky lines up to 97 per cent at the regions of the spectra with the least sky background noise.

| ID	RA [h m s]	Dec. [° ′ ″]	$z_{\rm spec}$	$F_{\rm [OII]}$ [10^{-20} W m^{-2}]	$L_{\rm [OII]}$ [10^{34} W]	EW_0 [Å]	SFR [M$_\odot$ yr^{-1}]	i'	L_K [L_K^*]
CVB13_1	02:18:04.411	-05:01:08.25	1.25427	4.8	4.4 ± 0.4	17	6.2 ± 1.8	22.480	3.5
CVB13_2	02:18:07.815	-04:59:17.22	1.26712	1.0	1.0 ± 0.4	25	1.3 ± 0.7	23.777	1.1
CVB13_3	02:18:06.449	-05:00:54.87	1.27453	1.2	1.1 ± 0.4	11	1.5 ± 0.7	23.292	2.1
CVB13_4	02:18:05.804	-05:00:50.10	1.27580	2.3	2.2 ± 0.4	16	3.1 ± 1.0	22.934	1.7
CVB13_5	02:18:06.826	-04:59:17.36	1.27605	2.8	2.7 ± 0.4	17	3.8 ± 1.2	23.772	1.8
CVB13_6	02:18:09.768	-05:00:31.80	1.28199	1.1	1.0 ± 0.1	11	1.5 ± 0.4	24.226	0.2
CVB13_7	02:18:15.069	-05:02:12.49	1.28338	2.5	2.4 ± 0.1	19	3.3 ± 1.0	22.693	1.3
CVB13_8	02:18:14.116	-05:01:12.02	1.28350	2.2	2.1 ± 0.1	23	3.0 ± 0.9	24.588	0.3
CVB13_9	02:18:08.568	-05:00:27.32	1.28517	10.1	9.9 ± 0.1	51	13.8 ± 4.0	23.610	0.3
CVB13_10	02:18:17.524	-05:00:34.91	1.28629	9.8	9.6 ± 0.1	20	13.4 ± 3.8	22.642	2.7
CVB13_11	02:18:16.661	-05:01:28.73	1.28676	1.5	1.5 ± 0.1	48	2.1 ± 0.6	26.278	0.5
CVB13_12	02:18:16.402	-05:02:08.13	1.40024	1.3	1.5 ± 0.5	18	2.1 ± 0.9	23.027	1.5
CVB13_13	02:18:25.450	-04:59:44.17	1.40508	1.5	1.8 ± 0.5	11	2.6 ± 1.0	23.371	3.1
CVB13_14	02:18:24.377	-04:59:54.12	1.41119	3.5	4.2 ± 0.1	46	5.9 ± 1.7	22.753	0.7
CVB13_15	02:18:15.406	-05:00:04.62	1.41120	5.6	6.9 ± 0.1	69	9.6 ± 2.8	24.243	0.2
CVB13_16	02:18:14.512	-05:01:10.79	1.41148	4.0	5.0 ± 0.1	38	6.9 ± 2.0	23.489	0.9
CVB13_17	02:17:59.932	-05:01:20.99	1.44405	4.3	5.6 ± 0.1	39	7.9 ± 2.3	23.875	0.8
CVB13_18	02:17:54.806	-05:02:03.29	1.45319	3.6	4.7 ± 0.1	87	6.6 ± 1.9	24.173	0.6
CVB13_19	02:18:12.424	-05:02:01.65	1.45331	7.4	9.7 ± 0.1	23	13.6 ± 3.9	23.012	3.4
CVB13_20*	02:17:57.251	-05:02:23.82	1.45349	1.6	2.1 ± 0.1	62	2.9 ± 0.8	23.484	3.9
CVB13_21	02:18:09.084	-05:00:27.58	1.45393	1.1	1.5 ± 0.1	11	2.1 ± 0.6	23.398	0.5
CVB13_22	02:18:03.930	-04:59:08.76	1.45479	4.2	5.5 ± 0.1	29	7.7 ± 2.2	23.600	1.0
CVB13_23	02:18:10.251	-05:00:24.12	1.45558	1.9	2.5 ± 0.1	23	3.4 ± 1.0	24.448	0.4
CVB13_24A	02:18:12.252	-05:01:11.44	1.46968	8.2	1.1 ± 0.1	91	15.5 ± 4.4	23.134	0.8
CVB13_24B	02:18:12.172	-05:01:11.65	1.47274	5.0	6.8 ± 0.1	43	9.5 ± 2.7	23.134	$\lesssim 0.3$
CVB13_25	02:18:06.292	-05:01:34.62	1.48464	5.7	7.9 ± 0.1	85	11.1 ± 3.2	23.606	1.1
CVB13_26	02:18:18.700	-05:01:10.74	1.48472	3.2	4.4 ± 0.1	43	6.2 ± 1.8	24.398	0.4
CVB13_27	02:18:16.859	-05:00:55.27	1.48896	4.0	5.6 ± 0.1	24	7.9 ± 2.3	23.809	2.3
CVB13_28	02:18:10.725	-05:00:22.11	1.49951	7.4	1.1 ± 0.1	57	14.6 ± 4.2	23.910	0.4
CVB13_29	02:18:21.719	-05:01:02.32	1.50186	3.3	4.7 ± 0.6	58	6.5 ± 2.0	24.033	1.4
CVB13_30	02:17:54.986	-05:01:32.49	1.53905	5.8	8.9 ± 0.6	29	12.4 ± 3.6	23.591	0.4

Table 1. Properties of the [O II] emitters. Column 1 states the galaxy ID; 24B was discovered serendipitously in the slit of 24A and does not meet the K-limit of the parent sample. The RA and Dec given in columns 2 and 3 are in equinox J2000. The (heliocentric) redshift and line flux of the emitters (columns 4 and 5) are derived from a double Gaussian fit to the [O II] 3727 Å line profile. The line luminosity is shown in column 6, and column 7 is the rest-frame equivalent width. Column 8 shows the star-formation rate derived from $L_{\rm [OII]}$ (following Kennicutt 1998) and column 9 is the i'-band magnitude (Vega). Column 10 shows the K-band luminosity in units of L^* at the galaxy's redshift, calculated with $M_K^* = -24.34$ (Lin et al. 2004) at $z = 0$ and assuming passive evolution (following prescriptions of Bruzual & Charlot [2003]) with a formation redshift of $z_{\rm form} = 4$. The error on the flux measurement is $\sim 1 \times 10^{-21}$ W m^{-2}, although in regions dominated by sky lines ($1.25 \lesssim z \lesssim 1.28$, $1.37 \lesssim z \lesssim 1.41$, and $z \gtrsim 1.5$) the error is on average four times higher. The error on the redshift measurement is estimated at 5×10^{-5}. The error on the luminosity is the propagated flux error. The error quoted for the SFR is the error derived from Eq. 1 and the error on the luminosity added in quadrature. *Observed with GMOS (see Van Breukelen et al. [in prep.]).

Fig. 5 (*left*) shows the redshift distribution of the 31 objects in our sample. Overplotted on the spectroscopic-redshift histogram is the expected number of [O II] emitters per redshift bin in our field, calculated with the observed Schechter luminosity function for [O II] emitters at $z = 1.47$ from Ly et al. (2006): $\log_{10}(\phi^*/{\rm Mpc}^{-3}) = -1.97 \pm 0.06$; $\log_{10}({\rm L}^*/{\rm W}) = 35.60 \pm 0.05$; $\alpha = -0.78 \pm 0.13$. The expected number of [O II] emitters is corrected by multiplying by the wavelength-dependent product of the three completeness factors, namely $0.25 \times 0.42 \times (0.22 - 0.97)$. Note that this implicitly assumes no correlation between [O II] flux and observed K-band magnitude. However, if for example the rest-frame equivalent width of the [O II] line is constant with the absolute blue magnitude of the galaxies, we would expect a positive correlation between [O II] flux and rest-frame blue magnitude. Therefore, if the colours of the [O II] emit-

ters are constant, we would expect a positive correlation between [O II] flux and observed K-band magnitude. This would make the completeness factor of 0.25 in point (i) an underestimate. On the other hand, if the colour term is bluer for galaxies with a higher star-formation rate – and hence brighter [O II] emission – then this would counter the positive correlation. Studies of [O II] emission at $z \sim 0 - 1$ (e.g. Hogg et al. 1998) do not allow us to separate these effects, so we adopt the 0.25 completeness factor and discuss the effects of extreme departures from this value in Section 3.3.

3.3 Evidence of clustering

The distribution of photometric redshifts in the field of CVB13 has a clear peak at $z = 1.4$, as is shown in Fig. 1. Spectroscopic follow-up however shows that the single
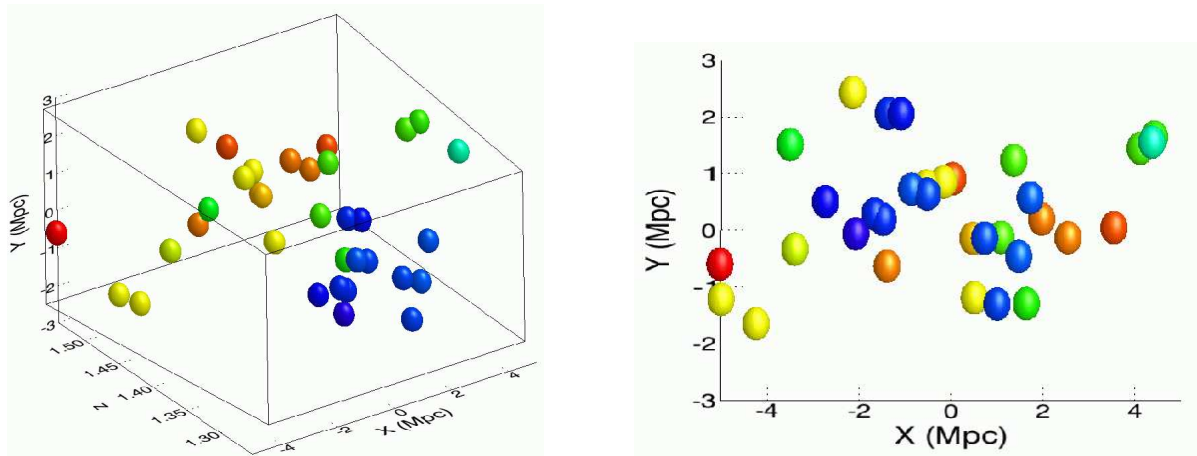
Figure 4. The three-dimensional distribution of galaxies within our spectroscopic sample (see Fig. 2: red circles) in comoving coordinates (X corresponds to RA, Y to Dec and z to redshift). The plotted box reflects the field of CVB13 as defined in section 2.3; the front and back faces are defined by the RA and Dec limits as described in the caption of Fig. 1. The galaxies are colour-coded to redshift, from blue at $z = 1.25$ to red at $z = 1.53$. *Right:* XY-projection of the galaxy distribution.
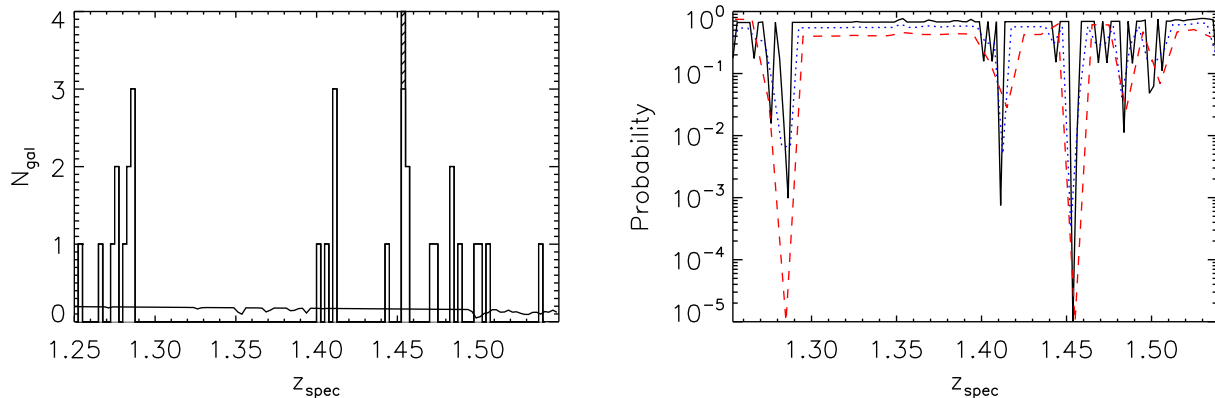

Figure 5. *Left:* histogram of the spectroscopic redshifts of the targeted galaxies with detected [O II] emission in the field of CVB13. The shaded bin represents the galaxy observed with GMOS. Overplotted is the expected number of [O II] emitters per redshift bin, taking into account our detection completeness (see section 3.2). The effects of the sky lines are somewhat smoothed in the plot owing to the binning of the histogram. *Right:* The probability of the detected number of [O II] emitters per redshift bin being due to the background model, using the method of Brand et al. (2003) described in Section 3.3. The solid black line is for a bin size of $\Delta z = 0.0025$, the dotted blue line for $\Delta z = 0.005$, and the dashed red line for $\Delta z = 0.01$.

redshift-peak at $z = 1.4$ separates into three less significant peaks at $z = 1.40$, $z = 1.45$, and $z = 1.48$, as pictured in Fig. 5 (*left*). There is also a clear overdensity at $z = 1.28$ which was not detected in the photometric redshift catalogue.

Following the method of Brand et al. (2003) we calculate the probability in each redshift bin (using Poissonian low-number statistics) that the number of [O II] emitters is greater than the number detected, given the number of [O II] emitters predicted by the model. The result is shown in Fig. 5 (*right*) for bin sizes of $\Delta z = 0.0025$ (120 bins, black solid line), $\Delta z = 0.005$ (60 bins, blue dotted line), and $\Delta z = 0.01$ (30 bins, red dashed line). For a bin size of $\Delta z = 0.01$ the redshift peaks at $z = 1.28$ and $z = 1.45$ both have a probability of 10^{-5}. As there are 30 bins with this bin size, one would expect to find such a low value in 0.03 per cent drawn from a set of random realizations. Based on these statistics we deem the structures at $z = 1.28$ and

$z = 1.45$ to be highly significant overdensities. Other peaks in the redshift distribution could reflect genuine structures but could alternatively be due to Poisson noise in the background distribution. Note that if the completeness factor of point (i) in Section 3.2 is smaller than 0.25, the overdensities would be even more significant; if the factor is larger than 0.25 this would reduce the probability of the two structures up to ~ 0.01 for a factor of 1. However, this large a completeness value is disproved by the existence of object CVB13_24B which has strong [O II] emission but $K > 20.6$, and by the occurence of similar high equivalent width objects in the sample of Hogg et al. (1998).

We do not detect any obvious signs of clustering in RA and Dec in our spectroscopic sample (see Fig. 4). This is principally because (i) we were unable to spectroscopically observe every photometric candidate cluster galaxy within the allocated time (ii) the MOS instrument was unable to completely sample the cluster core, as slitlets cannot be
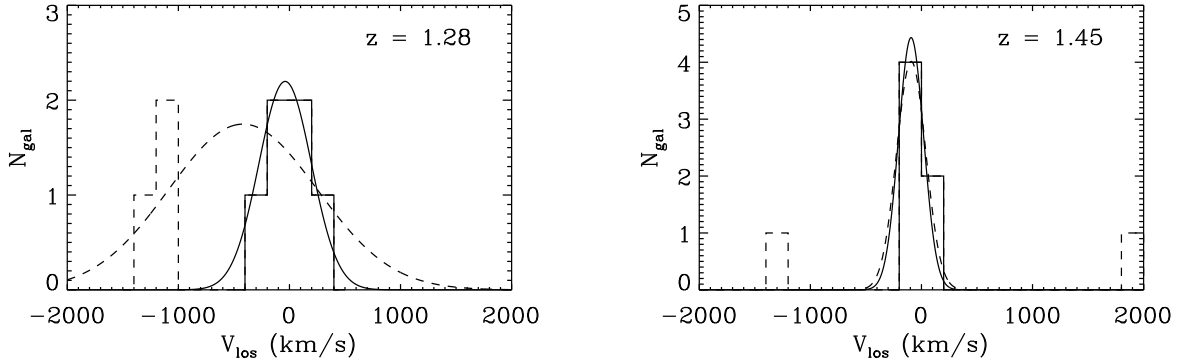
Figure 6. *Left:* The line-of-sight velocity distribution for the structure at $z = 1.28$. The solid lines in both the histogram and the fitted Gaussian comprise all galaxies within a range of ± 1000 km s^{-1} from the centre. The dashed lines show the sample within ± 2000 km s^{-1}. *Right:* Velocity distribution for the structure at $z = 1.45$. Line styles are as in the diagram on the left.

placed within $1.5''$ along the spatial axis, nor next to each other along the dispersion axis as the spectra will overlap, and (iii) we could only determine redshifts for [O II] emitting galaxies and not for the red, passively-evolving galaxies, which are customarily more clustered (e.g. Meneux et al. 2006).

3.4 Velocity dispersions and mass estimates

The line-of-sight velocity distribution of the two statistically robust structures at $z = 1.28$ and $z = 1.45$ is shown in Fig. 6. The bi-weighted mean of the redshifts and the 'gapper' estimate of the velocity dispersion are calculated for each of the structures, using the procedure outlined in Beers, Flynn & Gebhardt (1990). Subsequently, we estimate the masses of the groups using the relation between cluster mass M_{200} (the mass contained within a sphere of radius r_{200} for which the mean density is $200\,\rho_{\rm cr}$) and virial velocity found by Evrard (2004) (Eq. 2), substituting $\sigma_{\rm v} = \sqrt{3}\sigma_{v,\rm los}$:

$$M_{200} = \frac{10^{15}h^{-1}{\rm M_\odot}}{H/H_0}\left(\frac{\sqrt{3}\sigma_{\rm v,los}}{1080\,{\rm km\,s^{-1}}}\right)^3, \qquad (2)$$

where for a flat Universe:

$$H(z) = H_0\sqrt{\Omega_\Lambda + \Omega_{\rm M}(1+z)^3}. \qquad (3)$$

An alternative mass estimate is based on the stellar light of the groups observed in the K-band. This is done in a number of steps. First, we calculate the K-band luminosity of each galaxy in terms of L_K^* at the appropriate redshift. This parameter is determined by assuming $M_K^* = -24.34$ for the cluster luminosity function (Lin, Mohr & Stanford 2004) at $z = 0$, and passive evolution of the K-band luminosity function given a formation redshift of $z_{\rm form} = 4$. Next, we sum all the luminosities of the observed galaxies and correct for the missed fraction of light due to the flux limit, according to the luminosity function of Lin et al. (2004). To arrive at the total mass we then take a mass-to-light ratio of $(M/{\rm M_\odot})/(L/{\rm L_\odot})$ of $75h$ (Rines et al. 2001) which is assumed constant with redshift *in terms of L_K^** (note that assuming passive evolution of the luminosity function implies L_K^* itself increases with redshift). The mass thus estimated is only a lower limit, as we do not correct for the fact that

our spectroscopic sampling of the group members is most likely incomplete.

As is illustrated in Fig. 6 (*left*) the mean redshift and velocity dispersion of the structure at $z = 1.28$ is highly dependent on the limit imposed on the individual galaxy velocity for group membership. If we assume all galaxies within a range of 2000 km s^{-1} are members of the group, we obtain a mean redshift of $\overline{z} = 1.282 \pm 0.002$ and a velocity dispersion of $\sigma_{\rm v,los} = 668 \pm 149$ km s^{-1}. Placing the limit at 1000 km s^{-1} however gives $\overline{z} = 1.2847 \pm 0.0008$, $\sigma_{\rm v,los} = 236 \pm 63$ km s^{-1}. Assuming the group is virialised, the dynamically inferred masses are $5 \times 10^{14}{\rm M_\odot}$ and $3 \times 10^{13}{\rm M_\odot}$ respectively. The mass estimates from the total stellar light are $8 \times 10^{13}{\rm M_\odot}$ and $4 \times 10^{13}{\rm M_\odot}$ respectively for the two galaxy samples.

The structure at $z = 1.45$ gives similar velocity distributions for the samples in the two velocity ranges (see Fig. 6 [*right*]). We arrive at $\overline{z} = 1.4542 \pm 0.0004$ and $\sigma_{\rm v,los} = 113 \pm 57$ km s^{-1}; the inferred dynamical mass is only $5 \times 10^{12}{\rm M_\odot}$. The mass derived from the stellar light yields a much higher estimate of $9 \times 10^{13}{\rm M_\odot}$. Since we have spectroscopic confirmation for six to eight galaxies in the group with a total stellar mass of $1.6 - 1.8 \times 10^{12}{\rm M_\odot}$ we believe $\sim$ a few $10^{13}{\rm M_\odot}$ is a sensible minimum mass for the associated dark matter halo.

3.5 X-ray and radio properties

We have performed an analysis of the X-ray emission around CVB13. Fig. 7 (*left*) shows a three-colour ($Bi'K$) image of the central $3' \times 3'$ field with X-ray and radio (VLA B-array) contours overlaid. We detect X-ray emission at RA = $02^h18^m09^s$ and Dec = $-05°00'30''$ (object X2, see Table 2 and Ueda et al. [in prep] source no. 0712) which is coincident with the optical/near-infrared cluster position. The X-ray source appears extended with a deconvolved size of $\sim 5''$ (the XMM point spread function is $\sim 6''$). The total X-ray flux is $F_X = 9.1 \times 10^{-18}{\rm W\,m^{-2}}$, which would mean a luminosity of $L_X = 8.9 \times 10^{36}{\rm W}$ if the emission is associated with the cluster at $z = 1.28$ or $L_X = 1.2 \times 10^{37}{\rm W}$ at $z = 1.45$. This would be indicative of a cluster mass of $\sim 10^{14}{\rm M_\odot}$ for one of the clusters, or $\sim 8 \times 10^{13}{\rm M_\odot}$ each if
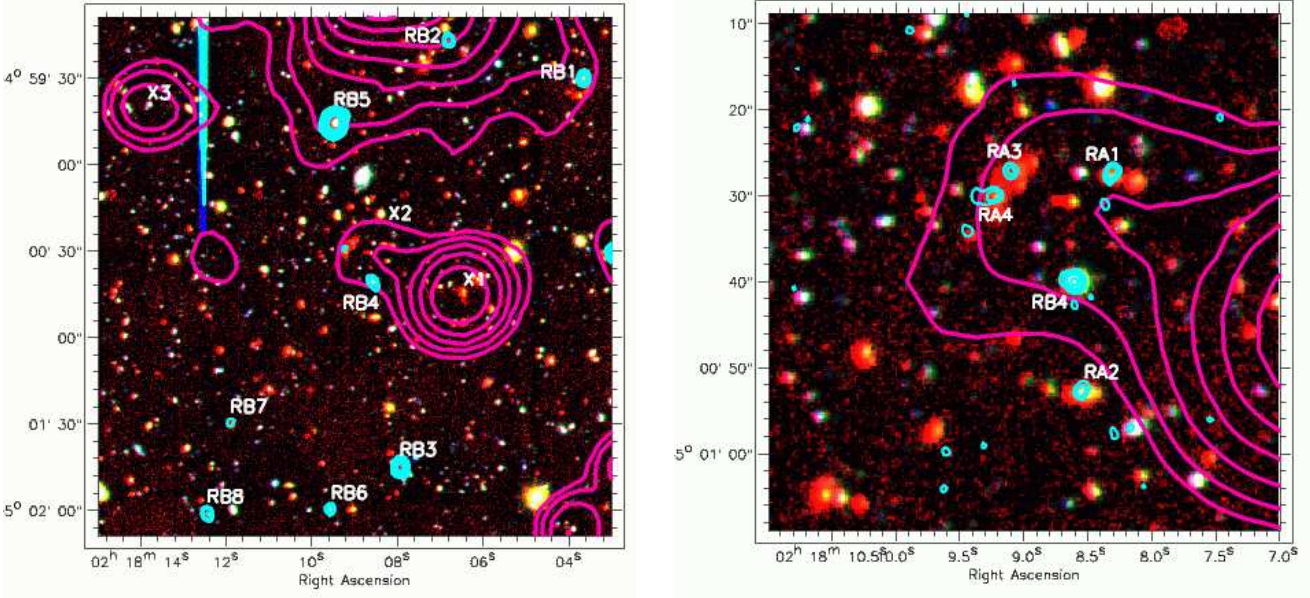
Figure 7. *Left:* $Bi'K$ colour image (Furusawa et al. [in prep.]) of the central $3' \times 3'$ region of CVB13. X-ray contours are from a signal-to-noise radio map in the 0.5 - 2 keV band and are overlaid in purple (contour levels at $[\sqrt{2}\sigma, 2\sigma, 2\sqrt{2}\sigma, ...]$); the 1.4-GHz VLA B-array radio map is contoured in blue (contour levels at $[4\sigma, 4\sqrt{2}\sigma, 8\sigma, ...]$). The radio beam size is $5'' \times 4''$ at PA $= 170°$. X-ray and radio sources are labelled as in Table 2. *Right:* Colour image as left, zoomed in on the central $1' \times 1'$ region. The radio contours are from the higher resolution VLA A-array radio map (contour levels at $[2\sqrt{2}\sigma, 4\sigma, 4\sqrt{2}\sigma, ...]$), with a beam size of $1.9''$ by $1.6''$ at PA $= 22°$.

ID	RA [h m s]	Dec. [° ′ ″]	F [W m^{-2}]	z_photo	z_spec	Ref.
X1	02:18:06.52	-05:00:43.9	$2.5 \pm 0.3 \times 10^{-17}$	1.06	-	
X2	02:18:08.37	-05:00:30.3	$9.1 \pm 2.1 \times 10^{-18}$	-	-	
X3	02:18:13.83	-04:59:39.2	$6.4 \pm 1.5 \times 10^{-18}$	-	1.258	Simpson et al. (in prep)
	[h m s]	[° ′ ″]	[μJy]			
RB1	02:18:03.66	-04:59:30.1	122 ± 26	1.05	-	
RB2*	02:18:06.83	-04:59:16.8	174 ± 50	1.11	1.276	This paper (CVB13_5)
RB3	02:18:07.94	-05:01:45.0	256 ± 27	-	-	
RB4	02:18:08.59	-05:00:40.0	102 ± 29	-	0.493	Simpson (priv. comm.)
RB5	02:18:09.48	-04:59:45.5	2347 ± 28	1.35	1.094	Simpson et al. (in prep)
RB6	02:18:09.55	-05:02:00.0	68 ± 22	-	1.268	Simpson (priv. comm.)
RB7	02:18:11.89	-05:01:29.6	49 ± 21	0.75	0.918	This paper
RB8	02:18:12.44	-05:02:01.3	104 ± 27	1.32	1.453	This paper (CVB13_19)
RA1	02:18:08.30	-05:00:27.2	67 ± 20	1.02	-	
RA2	02:18:08.57	-05:00:52.8	73 ± 30	0.94	-	
RA3	02:18:09.10	-05:00:27.2	66 ± 29	1.27	1.454	This paper (CVB13_21)
RA4	02:18:09.23	-05:00:30.0	109 ± 38	1.32	-	

Table 2. Table of the X-ray and radio sources in the $3' \times 3'$ central region of CVB13. The IDs correspond to the labels in Fig. 7. The RA and Dec are given in columns 2 and 3. The values in column 4 are the X-ray flux (0.5 - 10 keV) for the X-ray sources, and the 1.4-GHz radio flux density for the radio sources. The photometric redshifts (column 5) were determined as described in VB06. The spectroscopic redshifts (column 6) are from various sources as referenced in column 7. *This object appears to be a resolved source in the B-array data, but the A-array data shows that it actually consists of 3 separate objects. The central object on its own has a flux of $F = 113 \pm 24 \, \mu$Jy.

both clusters contribute equally to the X-ray flux (Reiprich & Böhringer 2002). The signal-to-noise ratio is too low to allow us to detect the 6.4 keV iron line and thus we cannot assign a secure redshift to the X-ray source. However, enough photons are detected in the source to conduct a crude hardness ratio (HR) spectral analysis. The HR-values

are HR2 $= (C_3 - C_2)/(C_2 + C_3) = 0.38 \pm 0.22$ and HR3 $= (C_4 - C_3)/(C_3 + C_2) = 0.01 \pm 0.16$ where C_2 is the 0.5 - 2.0 keV count rate, C_3 the 2.0 - 4.5 keV count rate, and C_4 the 4.5 - 10.0 keV count rate (Ueda et al. [in prep.]). These ratios mean the X-ray spectrum is much harder than typical for a cluster, and is more characteristic for an ab-

sorbed active galactic nucleus (e.g. Della Ceca et al. 2004). However, we do not find evidence for a single obscured AGN (e.g. a 24-μm or radio source) at the exact position of the X-ray emission. This is a puzzling system which is at face value an extended hard X-ray source. It requires an emission mechanism beyond any simple addition of a single obscured, non-thermal AGN and thermal cluster emission. Two such mechanisms that can cause the extended hard X-ray emission are inverse Compton scattering (see for example Fabian et al. 2006b) or confusion of more than one hard-spectrum X-ray source.

There is a significantly brighter X-ray source ~ 40 arcsec to the southwest of CVB13 (X1, see Fig. 7 [*left*]). It is uncertain if it is physically associated with the weaker extended X-ray emission; however it is certainly associated with a distant galaxy. A third X-ray source in the field (X3) is associated with an AGN at a redshift coincident with the $z = 1.28$ structure (see Table 2). Table 2 also shows the properties of the eight brightest radio sources in the field shown in Fig. 7 (*left*). There are radio sources associated with both the $z = 1.28$ and the $z = 1.45$ clusters, but the bright radio source RB4 closest to CVB13 is associated with a foreground galaxy at $z \sim 0.5$. In Fig. 7 (*right*) we plot a zoomed-in view of the CVB13 field and overplot the contours of the VLA A-configuration map. This confirms four weak radio sources tentatively seen in the B-configuration map (Fig. 7 [*left*]). One of these objects (RA3) has spectroscopically been confirmed to be at $z = 1.45$. RA4 has similar colours and photometric redshift and is therefore likely to be part of the same cluster. There is inconclusive evidence that the radio source associated with this galaxy has the 'head-tail' structure characteristic of galaxies moving with respect to an intracluster medium.

If the radio emission is solely due to synchrotron radiation from a starburst, the SFR of a radio source with a 1.4-GHz flux density of $100\,\mu$Jy is $\sim 1400\,\mathrm{M}_\odot\,\mathrm{yr}^{-1}$ in stars with masses of $> 5\,\mathrm{M}_\odot$ (see Condon 1992). Assuming a Salpeter IMF, this would mean a SFR$(M > 0.1\,\mathrm{M}_\odot)$ of $\sim 7000\,\mathrm{M}_\odot\,\mathrm{yr}^{-1}$. The SFR derived from the [O II] emission of these objects is only $\sim 10\,\mathrm{M}_\odot\,\mathrm{yr}^{-1}$, and although this estimate does not take extinction into account and is therefore a lower limit, the sub-millimetre SCUBA HAlf Degree Extragalactic Survey (SHADES, e.g. Coppin et al. 2006) covers this region and does not identify any highly obscured starbursts. If, on the other hand, all radio emission is ascribed to AGN activity we would expect (using Simpson et al. 2006, Eq. 9) a total X-ray luminosity of $\sim 10^{-16}\mathrm{W\,m}^{-2}$ in the 2 - 10 keV range. The object X2 only has a flux in this band of $\sim 10^{-17}\mathrm{W\,m}^{-2}$; therefore confusion between hard X-ray sources associated with the radio sources is a possible explanation for this seemingly extended hard X-ray source.

4 CONCLUDING REMARKS

We have obtained multi-object spectroscopy on a photometrically selected cluster candidate at $z = 1.4$. Instead of a single massive cluster, we find three projected structures of galaxies at $z = 1.40$, $z = 1.45$, and $z = 1.48$, one of which (at $z = 1.45$) is statistically robust. We also serendipitously detect a robust structure at $z = 1.28$. Both the structure at

$z = 1.45$ and the one at $z = 1.28$ have masses $\sim 10^{14}\mathrm{M}_\odot$ and may therefore be termed poor galaxy clusters.

The evolutionary status of both the $z = 1.28$ and $z = 1.45$ clusters is uncertain. The cluster at $z = 1.45$ has a significantly lower virial mass than its mass derived from the total observed luminosity. It is very likely that this structure is not yet virialised, which would suppress the derived (three-dimensional) velocity dispersion of $\sim 200\,\mathrm{km\,s}^{-1}$. The velocity shear (half-width to zero intensity) observed in CVB13_21 - located centrally within the cluster - is $320\,\mathrm{km\,s}^{-1}$, which shows that the measured velocity dispersion of the cluster is unlikely to represent the total cluster mass. Note however that low-number statistics make an accurate determination of the velocity dispersion unfeasible. The total measured SFRs are ~ 45 and $\sim 60\,\mathrm{M}_\odot\,\mathrm{yr}^{-1}$ respectively for the clusters at $z = 1.28$ and $z = 1.45$, which for a mass of $\sim 1 \times 10^{14}\mathrm{M}_\odot$ within $4 \times 4 \times 4\,\mathrm{Mpc}^3$ (comoving) is a factor of 3 - 5 higher than typical star-formation rates observed in the field at these redshifts (e.g. Conolly et al. 1997)

The analysis of the cluster galaxies in this paper is based solely on redshifts estimated from [O II] emission line features. Therefore the overdensities we find at $z = 1.28$ and $z = 1.45$ only consist of star-forming galaxies, whereas the candidate cluster found by VB06 was selected with a photometric redshift algorithm which is sensitive to red, passively-evolving galaxies. Of the 18 highest-priority targets of sample 1, 10 were observed, and only six redshifts were obtained, two of which were confirmed to be cluster members. The other galaxies were all priority 3 targets of sample 1. We suspect there will be an appreciable number of red galaxies in the cluster that we were unable to confirm spectroscopically. More observations of the central cluster galaxies, specifically for the cluster at $z = 1.45$, may also produce a higher velocity dispersion measurement. To thoroughly understand the nature and masses of the structures, we need to be able to obtain redshifts for this type of galaxy as well. Deep, near-infrared spectroscopy, for example with the Fibre Multi Object Spectrograph (FMOS, Dalton et al. 2006), will give a more complete sample and therefore yield a more comprehensive result for high-redshift galaxy clusters.

The extended X-ray luminosity at the position of these structures is characteristic of a cluster with a mass of $\sim 10^{14}\mathrm{M}_\odot$. However the X-ray spectrum is too hard to simply be caused by thermal cluster gas emission. A non-thermal effect like inverse Compton scattering could cause an X-ray detection with a spectral shape reflecting the energy distribution of the underlying electron population. The most likely explanation, however, is confusion caused by more than one AGN contributing to the X-ray emission. To shed light on the exact nature of this system, it will be interesting to study the cluster gas via the Sunyaev-Zel'dovich effect and the dark-matter mass via lensing.

The original mass estimate of CVB13 by VB06 of $3 \times 10^{14}\mathrm{M}_\odot$ is likely to be overestimated due to the superposition of the two lower-mass structures at $z = 1.40$ and $z = 1.48$. The single structure at $z = 1.28$ contains too few galaxies to be isolated by the same selection algorithm. This result suggests that spectroscopic follow-up is a vital element of photometric cluster surveys as the latter are prone to projection effects and can seriously overestimate cluster masses. To determine the impact of these effects, we

calculate the probability of finding three groups in projection within $\Delta z = 0.1$ in a survey such as the one presented in VB06. Assuming a Sheth-Tormen cluster mass function (Sheth & Tormen 1999) we expect to find 121 groups with masses of a few $10^{13} M_\odot$ and 6 clusters with masses of $\sim 10^{14} M_\odot$ within the redshift range $1.25 \leqslant z \leqslant 1.55$ in a field of 0.5 deg^2. Neglecting spatial clustering of the groups, there are on average two superpositions of three groups with masses $\sim 10^{13} M_\odot$ within a box of 2 x 2 Mpc^2 and $\Delta z = 0.1$. The probability of finding a projection of two groups and one cluster of $\sim 10^{14} M_\odot$ (as for CVB13) is 45 per cent. Running the cluster algorithm of VB06 on a simulated superposition of three groups shows that in order to distinguish between massive clusters at this redshift and projected groups with a redshift separation of $\Delta z = 0.05$, the photometric redshift error needs to be as small as $\frac{\sigma_z}{1+z} = 0.005$. The COMBO-17 survey (Wolf et al. 2004), which determined photometric redshifts from photometry in 17 bands, obtained a best redshift error of $\frac{\sigma_z}{1+z} = 0.01$ for galaxies with $R < 21$ (c.f. $R \sim 24$ for CVB13 targets). Thus attaining the order of accuracy needed in photometric redshifts to determine the cluster mass function at high redshifts seems very challenging, and we caution against attempting this with photometric techniques alone.

5   ACKNOWLEDGMENTS

REFERENCES

Abell G. O., 1958, ApJS, 3, 211
Abell G. O., Corwin H. G., Olowin R. P., 1989, ApJS, 70, 1
Beers T. C., Flynn K., Gebhardt K., 1990, AJ, 100, 32
Birkinshaw M., 1999, Phys. Rept. 310, 97
Bower R. G., Lucey J. R., Ellis R. S., 1992, MNRAS, 254, 601
Brand K., Rawlings S., Hill G. J., Lacy M., Mitchell E., Tufts J., 2003, MNRAS, 344, 283
Bremer M. N. et al., 2006, MNRAS, 371, 1427
Bruzual G., Charlot S., 2003, MNRAS, 344, 1000
Carlstrom J. E., Joy M. K., Grego L., Holder G. P.,

Holzapfel W. L., Mohr J. J., Patel S., Reese E. D., 2000, Physica Scripta Volume T 85, 148
Cirasuolo M. et al., 2006, MNRAS, in press (astro-ph/0609287)
Cole S., 1991, AJ, 367, 45
Condon J. J., 1992, ARA&A, 30, 575
Conolly A. J., Szalay A. S., Dickinson M., Subbarao M. U., Brunner R. J., 1997, ApJ, 486, L11
Coppin K. et al., 2006, MNRAS, 372, 1621
Cotter G. et al., 2002, MNRAS, 331, 1
Cowley D. J., Faber S., Hilyard D. F., James E., Osborne J., 1997, SPIE, 2871, 1107
Dalton G. et al, 2006, SPIE, 6269, 136
Danese L., de Zotti G., di Tullio G., 1980, A&A, 82, 322
Della Ceca R. et al., 2004, A&A, 428, 383
Evrard A. E., 2004, in Mulchaey J. S., Dressler A., Oemler A., eds, Carnegie Astrophysics Series, Vol. 3
Fabian A. C., Celotti A., Erlund M. C., 2006a, MNRAS, 373L, 16
Fabian A. C., Sanders J. S., Crawford C. S., Ettori S., 2006b, MNRAS, 341, 729
Gladders, M. D. & Yee, H. K. C., 2005, ApJS, 157, 1
Gladders M. D., Lopez-Cruz O., Yee H. K. C., Kodama T., 1998, ApJ, 501, 571
Goto et al., 2002, AJ, 123, 1807
Heckman T. M., 2002, in Mulchaey J. S., Stocke J., eds, ASP Conf. Ser. 254: Extragalactic Gas at Low Redshift, pp. 292-+
Hogg D. W., Cohen J. G., Blandford R., Pahre M. A., 1998, ApJ, 504, 622
Hook I., Jørgensen I., Allington-Smith J. R., Davies R. L., Metcalfe N., Murowinski R. G., Crampton D., 2004, PASP, 116, 425
Ivison R. J. et al., 2007, MNRAS, in press (astro-ph/0702544)
Jones et al., 2005, MNRAS, 357, 518
Kennicutt R. C., 1998, ARAA, 36, 189
Kim R. S. J. et al., 2002, AJ, 123, 20
Kneissl R., Jones M. E., Saunders R., Eke V. R., Lasenby A. N., Grainge K., Cotter G., 2001, MNRAS, 328, 783
Lawrence et al., 2006, preprint (astro-ph/0604426)
Lin Y.-T., Mohr J. J., Stanford S. A., 2004, ApJ, 610, 745
Lobo C., Iovino A., Lazzati D., Chincarini G., 2000, A&A, 360, 896
Lonsdale C. J. et al., 2005, PASP, 115, 897
Ly C. et al., 2006, ApJ, 657, 738
Meneux B. et al., 2006, A&A, 452, 387
Miller C. J. et al., 2005, AJ, 130, 968
Osterbrock D. E., 1967, PASP, 79, 523
Pascarelle S. M., Windhorst R. A., Driver S. P., Ostrander E. J., Keel W. C., 1996, ApJ, 456, L21
Postman, M., Lubin, L. M., Gunn, J. E., Oke, J. B., Hoessel, J. G., Schneider, D. P. & Christensen, J. A., 1996, AJ, 111, 615
Reiprich T. H. & Böhringer H., 2002, ApJ, 567, 716
Rines K., Geller M. J., Kurtz M. J., Diaferio A., Jarrett T. H., Huchra J. P., 2001, ApJ, 561, L41
Rosati P. et al., 2004, AJ, 127, 230
Röttgering H. J. A., West M. J., Miley G. K., Chambers K. C., 1996, A&A, 307, 376
Scannapieco E., Oh S. P., 2004, preprint (astro-ph/0401087)

Sheth R. & Tormen G., 1999, MNRAS, 308, 119

Simpson et al., 2006, MNRAS, 372, 741

Stanford S. A., Bradford H., Rosati P., Tozzi P., Borgani S., Eisenhardt P. R., Spinrad H., 2001, ApJ, 552, 504

Stanford S. A. et al., 2006, ApJ, 646L, 13

Sunyaev R. A., Zeldovich Y. B., 1970, ASS, 7, 3

Sunyaev R. A., Zeldovich Y. B., 1972, Comments on Astrophysics, 4, 173

Van Breukelen C. et al., 2006, MNRAS, 373L, 26

Venemans B. et al., 2002, ApJ, 569L, 11

Watson M. G., Ueda Y., Akiyama M., Sekiguchi K. and the SXDS Collaboration, 2004, BAAS, 36, 1202 Smith A., 2000, in Minh Y. C., van Dishoeck E. F., eds, Proc. IAU Symp. 197, Astrochemistry: from molecular clouds to planetary systems. Astron. Soc. Pac., San Francisco, p. 210

White S. D. M., Frenk C. S., 1991, AJ, 579, 16

Wolf C. et al., 2004, A&A, 421, 913